

1 **Heat distribution in the Southeast Pacific is only**
2 **weakly sensitive to high-latitude heat flux and wind**
3 **stress**

4 **Daniel C. Jones¹, Emma Boland¹, Andrew J.S. Meijers¹, Gael Forget², Simon**
5 **A. Josey³, Jean-Baptiste Sallee⁴, and Emily Shuckburgh^{1,5}**

6 ¹British Antarctic Survey, Natural Environment Research Council, Cambridge, UK

7 ²Massachusetts Institute of Technology, Cambridge, MA, USA

8 ³National Oceanography Centre, Southampton, UK

9 ⁴L'Ocean, CNRS, UPMC, Paris, France

10 ⁵University of Cambridge, UK

11 **Key Points:**

- 12 • The heat content of the recently ventilated Pacific (RVPh) is strongly controlled
13 by gyre circulation.
- 14 • On timescales shorter than 3-5 years, RVPh is most sensitive to mid-latitude wind
15 stress anomalies.
- 16 • On timescales longer than 3-5 years, RVPh is most sensitive to mid-latitude heat
17 flux anomalies.

Corresponding author: D.C. Jones, dannes@bas.ac.uk

18 **Abstract**

19 The Southern Ocean features regionally-varying ventilation pathways that trans-
 20 port heat and carbon from the surface ocean to the interior thermocline on timescales
 21 of decades to centuries, but the factors that control the distribution of heat along these
 22 pathways are not well understood. In this study, we use a global ocean state estimate
 23 (ECCOv4) to (1) define the recently ventilated interior Pacific (RVP) using numerical
 24 passive tracer experiments over a 10-year period and (2) use an adjoint approach to cal-
 25 culate the sensitivities of the RVP heat content (RVPh) to changes in net heat flux and
 26 wind stress. We find that RVPh is most sensitive to local heat flux and wind stress anoma-
 27 lies north of the sea surface height contours that delineate the Antarctic Circumpolar
 28 Current, with especially high sensitivities over the South Pacific Gyre. Surprisingly, RVPh
 29 is not especially sensitive to changes at higher latitudes.

30 We perform a set of step response experiments over the South Pacific Gyre, the sub-
 31 duction region, and the high-latitude SO. In consistency with the adjoint sensitivity fields,
 32 RVPh is most sensitive to wind stress curl over the subtropical gyre, which alter isopy-
 33 cnal heave, and it is only weakly sensitive to changes at higher latitudes. Our results sug-
 34 gest that despite the localized nature of mode water subduction hotspots, changes in basin-
 35 scale pressure gradients are an important controlling factor on RVPh. Because basin-
 36 scale wind stress is expected to change in the coming decades to centuries, our results
 37 may have implications for climate, via the atmosphere/ocean partitioning of heat.

38 **1 Introduction**

39 The Southern Ocean (SO), defined here as the ocean south of 30°S, accounts for
 40 43%±3% of the oceanic component of anthropogenic carbon dioxide uptake and 75%±
 41 22% of oceanic heat uptake over the period 1861-2005, despite only occupying 30% of
 42 global surface ocean area (Frölicher et al., 2015). The SO’s ability to absorb and sequester
 43 this high fraction of heat and carbon comes from a combination of powerful overlying
 44 winds, strong buoyancy fluxes, seasonally-refreshed pools of weak stratification, and steeply
 45 tilted isopycnals that set up a pathway from the surface ocean into the interior thermo-
 46 cline (Speer et al., 2000; Hanawa & Talley, 2001; Russell et al., 2006; Lumpkin & Speer,
 47 2007; Talley, 2008; Herraiz-Borreguero & Rintoul, 2011; Speer & Forget, 2013). Heat and
 48 carbon anomalies are subducted in the pools of weak stratification, referred to collec-

49 tively as pools of Subantarctic Mode Water (SAMW), where they can be exported into
50 the interior via lateral induction, eddy-induced transport, and advection via the mean
51 flow, ventilating the subtropical thermocline on timescales of decades to centuries, with
52 significant regional variability (Karsten & Marshall, 2002; Sarmiento et al., 2004; Sabine
53 et al., 2004; Iudicone et al., 2007; Khatiwala et al., 2009; J.-B. Sallée et al., 2010; Ito et
54 al., 2010; J. Sallée et al., 2010; J. Sallée & Rintoul, 2011; Liu & Huang, 2012; J.-B. Sallée
55 et al., 2012; Cerovecki et al., 2013; Jones et al., 2016). Here, ventilation refers to the set
56 of processes by which surface ocean properties are able to affect the properties of the in-
57 terior ocean; it can be considered a consequence of the global ocean’s overturning cir-
58 culation (Marshall & Speer, 2012a; Cerovečki & Mazloff, 2015).

59 Despite recent efforts to better understand the regionally specific nature of sub-
60 duction and ventilation (e.g. Cerovecki et al. (2013); Jones et al. (2016)), we still have
61 relatively little knowledge on how regional variations in surface forcing and surface ocean
62 properties can ultimately impact subduction and the properties of the ventilated region.
63 We need a more sophisticated understanding of how changes in the location, magnitude,
64 and variability of surface forcing can impact this critical aspect of the overturning cir-
65 culation. Improvements in this area may be especially helpful for improving projections
66 of future ocean states, as changes in the Southern Ocean forcing-subduction-ventilation
67 mechanism are expected to have a considerable impact on future climate (Cessi & Oth-
68 eguy, 2003; Downes et al., 2009; Lovenduski & Ito, 2009; Morrison et al., 2011; J.-B. Sallée
69 et al., 2012).

70 In order to quantify how regional variations in surface forcing (e.g. net heat flux,
71 wind stress) may affect the heat distribution in the ventilated interior ocean, we perform
72 a set of adjoint sensitivity experiments in an observationally-constrained state estimate
73 (i.e. ECCOV4). Our adjoint model produces linear sensitivity fields that feature both
74 spatial and temporal variability, allowing us to identify the specific locations and timescales
75 on which surface forcing anomalies can eventually have especially large impacts on the
76 heat distribution in the ventilated interior. We then use the linear adjoint sensitivity fields
77 to inform the design of several non-linear step response experiments, allowing us to test
78 the validity of the adjoint predictions and to better understand the chain of mechanisms
79 involved in both the linear and non-linear responses of the Southern Ocean to changes
80 in heat flux and wind stress forcing.

81 Generally, on a selected timescale (e.g. 1 year, 10 years), we can consider the vol-
82 ume of the ocean that has been affected by near-surface properties (e.g. the tempera-
83 ture and salinity characteristics of the mode water formation regions) as having been “ven-
84 tilated” by advection and mixing. The ventilated volume sits below the mixed layer, such
85 that it is isolated from immediate contact with the surface. This view of ventilation is
86 more general than one that focuses on a specific water mass (e.g. SAMW), although there
87 is significant overlap with the water mass view. In this paper, we consider possible in-
88 fluences on the heat distribution of the ventilated volume in the Eastern Pacific sector
89 of the Southern Ocean, as defined by a set of numerical passive tracer release experiments
90 carried out in ECCOv4. We focus on the Eastern Pacific ventilated volume in partic-
91 ular because it is an especially efficient export pathway of water from the surface ocean
92 into the interior thermocline, as measured by the passive tracer advection rate in numer-
93 ical experiments (Jones et al., 2016). For convenience, we refer to the recently ventilated
94 interior Eastern Pacific as the RVP and the heat content of the RVP as RVP_h. Although
95 there is overlap between the two, we note that the RVP is more general than the SAMW
96 or any other particular water mass. Because RVP_h is fixed in volume for each adjoint
97 experiment, it is a measure of the heat distribution in the target region, as it can be af-
98 fected by both isopycnal heave that moves heat into and out of the RVP and by along-
99 isopycnal heat transport.

100 In section 2, we describe the ECCOv4 model setup, our definition of the recently
101 ventilated Pacific, and the design of our adjoint sensitivity experiments. In section 3, we
102 present the results of both the adjoint sensitivity experiments and the forward, non-linear
103 wind stress step response experiments. In section 4, we relate our results to other areas
104 and explore uncertainties. In section 5, we offer a brief summary and conclusions.

105 **2 Methods**

106 In section 2.1, we briefly describe the ECCOv4 global ocean state estimate used
107 in this work. In section 2.2, we describe how the control volume, i.e. the recently ven-
108 tilated Southeast Pacific, is defined, and in section 2.3, we describe the design of the ad-
109 joint sensitivity experiments.

2.1 The ECCOv4 state estimate

We use the modelling setup associated with ECCOv4 (release 2, hereafter ECCOv4-r2 or just ECCOv4). ECCOv4 is a *state estimate*, meaning that it has been adjusted to minimize the misfits between the model state and a suite of observations from various sources over the time period 1992-2011 (e.g. Argo temperature and salinity profiles, ship hydrography, satellite altimetry). No artificial sources or sinks of heat were used in the ocean interior; only the model’s initial conditions, surface forcing fields, and mixing parameters have been adjusted in order to reduce model-data misfit. The model setup is available for download on GitHub.com (<https://github.com/gaelforget/ECCOv4>) as an instance of the open source MIT general circulation model (MITgcm, <http://mitgcm.org/>, also available on GitHub). We briefly describe the relevant features of the ECCOv4 setup below; a more thorough description is available in Forget, Campin, et al. (2015) and references therein.

ECCOv4 is a global ocean model that uses a Lat-Lon-Cap (LLC) grid referred to as LLC90. Its horizontal grid size ranges from around 40-50 km at high latitudes up to roughly 110 km at the equator. It features parameterised diffusion, including both diapycnal and isopycnal components, simple convective adjustment, and the GGL mixed layer turbulence closure scheme (Gaspar et al., 1990). To represent the along-isopycnal effect of unresolved eddies, Forget, Campin, et al. (2015) used a bolus transport parameterization (Gent & McWilliams, 1990, hereafter GM). Although the horizontal resolution of ECCOv4 is relatively coarse (roughly 1°), its mixing properties are in good agreement with observations, thanks in part to the use of optimized, spatially-varying turbulent transport coefficients (Forget, Ferreira, & Liang, 2015). ECCOv4 features fully interactive dynamic sea ice, so that buoyancy and mass fluxes at the sea surface are recalculated based on the thermodynamic balance of Losch et al. (2010). Open ocean rain, evaporation, and runoff simply carry (advect through the free surface) the local SST and a salinity value of zero, and runoff is provided by a monthly climatology (Fekete et al., 2002). ECCOv4 calculates buoyancy, radiative, and mass fluxes using the bulk formulae of Large and Yeager (2009) with 6-hourly ERA-Interim re-analysis fields (Dee et al., 2011) as a “first guess” for the forcing fields. Specifically, we use wind stress, 2 m air temperature, 2 m specific humidity, wind speed, downward longwave radiation, and downward shortwave radiation as model inputs. These atmospheric state fields have been iteratively adjusted by the state estimation process in order to minimize model-data mis-

143 fits. The ECCOv4-r2 setup that we use here does *not* use surface salinity restoring. For
 144 additional validation information, see the online supporting information and Forget, Campin,
 145 et al. (2015).

146 **2.2 The control volume**

147 We use a combination of physical state variables and numerical passive tracer dis-
 148 tributions to identify the recently ventilated interior ocean in our global model. We ini-
 149 tialize passive tracer in selected areas with weak stratification (i.e. low values of poten-
 150 tial vorticity) at the base of the mixed layer, using a mixed layer definition based on the
 151 density change associated with a temperature variation $\Delta T = 0.8^\circ\text{C}$ (Kara & Rochford,
 152 2003). Specifically, we initialize the tracer in regions with September-October mean mixed
 153 layer depths greater than 300 m (Figure 1, green dashed lines) with PV values smaller
 154 than an annual minimum PV threshold. We initialize the tracer from the surface down
 155 to the annual maximum mixed layer depth. We integrate the tracer equations forward
 156 for 10 years, in “online” mode simultaneously with the momentum, buoyancy, and phys-
 157 ical tracer equations. Note that although the bulk of the tracer originates in the Pacific,
 158 a smaller fraction also comes from the Indian and Atlantic sectors. All releases start on
 159 1 January; our method of initializing tracer above the annual maximum mixed layer depth
 160 ensures that variations with seasonal release timings are minimal. We release the tracer
 161 in six different ensemble runs, with release years from 1996 to 2001. In order to define
 162 the RVP, we use the 10-year integrated tracer distribution and some additional phys-
 163 cal and geographical criteria, selecting grid cells that satisfy the following four conditions:

- 164 • be located below the maximum mixed layer over the entire ECCOv4-r2 period (1992-
 165 2011)
- 166 • time-integrated tracer concentration is at least 10% of the global ocean maximum
 167 value
- 168 • be located in the Southeast Pacific, between 170°W - 60°W and 60°S - 20°S
- 169 • potential density is greater than or equal to $26.9\sigma_0$

170 The resulting control volume is located roughly between 300-500m; the areal extent of
 171 the RVP changes with depth, reaching its maximum areal extent between 500-700m, cov-
 172 ering a large fraction of the South Pacific Gyre (Figure 1). For more information on the

173 tracer experiments and the resulting distribution, see our companion paper. Next, we
 174 examine the sensitivity of the heat content of the RVP to net heat flux and wind stress.

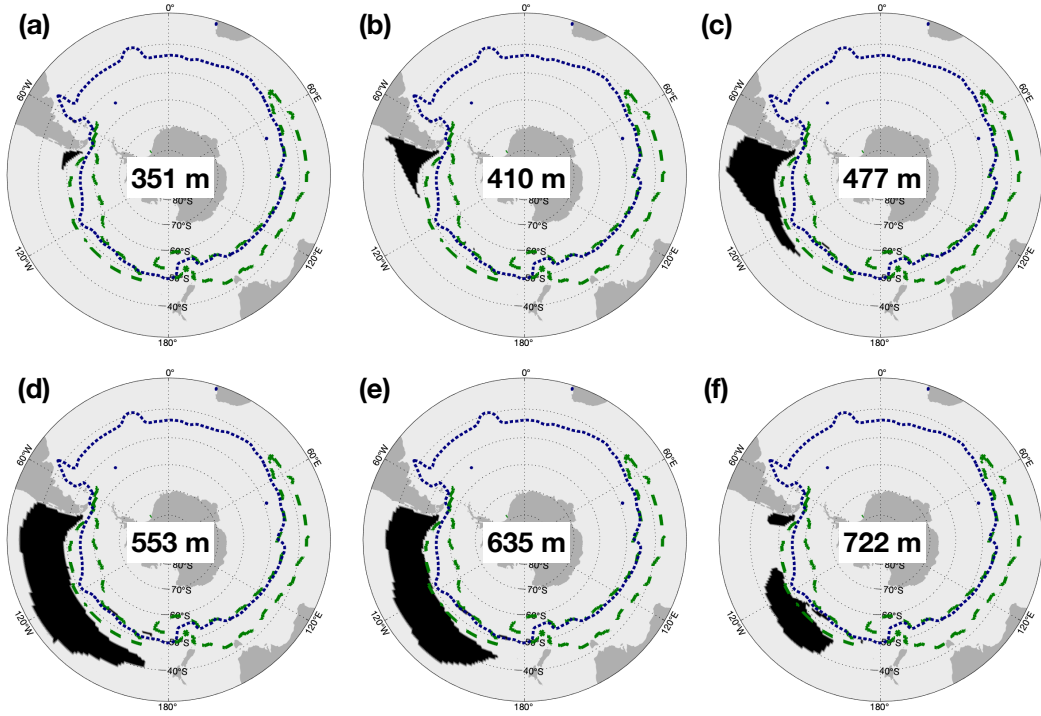


Figure 1. The vertical structure of the ensemble median recently ventilated Pacific (RVP), which is used as the control volume in this study (black). For reference, we also plot the lateral extent of the tracer release sites (green dashed lines), and the 1992-2011 mean position of the -0.25 m sea surface height contour, which is used as a proxy for the Subantarctic Front (blue dotted line). Depths indicate the depths of the grid cell centers.

175 **2.3 Adjoint sensitivity experiments**

176 In order to examine the sensitivity of RVP_h to interior ocean properties and sur-
 177 face forcing, we perform a set of adjoint sensitivity experiments. The objective function
 178 is defined as the annual- and volume-mean RVP heat content:

$$\tilde{J} = \frac{1}{V\Delta t} \int_V \int_{\Delta t} \rho_0 c_p \theta(\mathbf{r}, t) dt dV, \quad (1)$$

179 where ρ_0 is the reference density, c_p is the heat capacity of seawater, θ is the potential
 180 temperature, \mathbf{r} is the position vector, t is the time, V is the control volume, and Δt is
 181 the time period of the integration. For convenience, we scale \tilde{J} by the constant $\rho_0 c_p$, so
 182 RVP_h = $J = \tilde{J} / \rho_0 c_p$, meaning that RVP_h has units of $^{\circ}C$.

183 We compute an ensemble of six 14-year adjoint sensitivity experiments, with the
 184 objective function defined over the last year of each run, i.e. from 1 January to 31 De-
 185 cember, with years ranging from 2006 to 2011. We allow the RVP to vary between ex-
 186 periments, which represents less than a 10% change in volume across the ensemble. Our
 187 ECCOv4 adjoint model calculates the sensitivities of these objective functions to a large
 188 set of independent variables, including temperature ($\partial J/\partial T$), salinity ($\partial J/\partial S$), net heat
 189 flux ($\partial J/\partial q$), and wind stress ($\partial J/\partial \tau_x, \partial J/\partial \tau_y$). We also calculated the sensitivities to
 190 evaporation minus precipitation minus runoff ($E - p - r$), but we found the sensitivi-
 191 ties, when scaled by 14-day forcing anomalies relative to the 1992-2011 average, to be
 192 negligibly small compared with the other fields. We do not consider ($E - p - r$) fur-
 193 ther. We use 14-day averaged sensitivity fields throughout.

194 **3 Results**

195 We begin by examining the sensitivity of RVPh to net heat flux and wind stress
 196 forcing. We further examine the response mechanisms involved in the sensitivities to heat
 197 flux and wind stress using step response experiments.

198 **3.1 Sensitivity to net heat flux**

199 We now examine the sensitivity of RVPh to surface forcing, starting with net heat
 200 flux. We use the convention that positive heat flux is *out* of the ocean, i.e. positive flux
 201 tends to cool the surface ocean. The sensitivity fields calculated by the ECCOv4 setup
 202 are three-dimensional, as the sensitivity fields change with latitude, longitude, and time.
 203 We scale the 14-day mean sensitivities by convolving the sensitivities with 14-day mean
 204 surface forcing anomalies, where the anomalies are calculated relative to the 20-year mean
 205 ECCOv4 state. As we only remove a constant value at each grid cell, the forcing anoma-
 206 lies feature temporal variability on scales from 14-day to 20-year, including a seasonal
 207 cycle. Using this scaling, we can estimate the linear impacts of actual forcing anoma-
 208 lies on RVPh. For the unscaled sensitivity fields, see the online supporting information.
 209 The linear change in J expected from a forcing anomaly is:

$$\Delta J(\mathbf{r}, t) = \left[\frac{\partial J}{\partial x}(\mathbf{r}, t) \right] [x(\mathbf{r}, t) - \bar{x}(\mathbf{r})], \quad (2)$$

210 where \bar{x} is the mean value of the forcing field over the ECCOv4-r2 period. Clearly the
 211 sign of ΔJ is determined by the product of the sign of the sensitivity field and the sign

212 of the anomaly, such that positive and negative scaled sensitivities can potentially come
 213 from heat flux out of the ocean *or* heat flux into the ocean, depending on the sign of the
 214 sensitivity fields. The anomaly fields $x(\mathbf{r}, t) - \bar{x}(\mathbf{r})$ are averaged over 14-day periods in
 215 order to match the temporal averaging scale of the sensitivity fields.

216 The scaled sensitivities of RVP_h to net heat flux indicate the eventual estimated
 217 change in RVP_h induced by the net heat flux anomalies, as predicted by the adjoint sen-
 218 sitivities (Figure 2). The sensitivities display a marked contrast between Austral win-
 219 ter and Austral summer. In Austral winter, we find the largest scaled sensitivities just
 220 north of the SAF proxy, partially overlapping regions of deep mixed layers and the as-
 221 sociated formation of SAMW. As the unscaled sensitivities are largely negative every-
 222 where across all lags, the seasonal contrast in the sign of the scaled sensitivities comes
 223 from the sign of the net heat flux itself, with heat loss in the Austral winter and heat
 224 gain in the Austral summer. Regions of positive scaled sensitivity indicate a tendency
 225 for the actual net heat flux anomalies to *increase* RVP_h, whereas regions of negative scaled
 226 sensitivity indicate a tendency for the actual net heat flux anomalies to *decrease* RVP_h.
 227 Unscaled sensitivities are shown in the supporting information.

228 At longer lags (e.g. Figure 2a), the scaled sensitivities extend throughout the Pa-
 229 cific basin to New Zealand, illustrating that the RVP is sensitive to anomalous heat fluxes
 230 in upstream regions, given sufficient time for those anomalies to propagate into the RVP.
 231 For shorter lags, (e.g. Figure 2e), the scaled sensitivities are more local. In Austral sum-
 232 mer, the scaled sensitivities are much smaller and tend to be positive, indicating a lin-
 233 ear warming of the RVP; it is possible to warm the RVP by heating waters upstream of
 234 water formation regions. The Austral winter sensitivity is stronger at 6 years than 10
 235 years in the SE Pacific sector (Figure 2a-c) while the Austral summer sensitivity is strongest
 236 at 10 years. This may be indicative of a difference in the dominant processes between
 237 the two seasons, with summer solar forcing having a delayed impact on RVP properties
 238 compared to winter latent heat loss. We explore this idea further using heat flux per-
 239 turbation experiments in Section 3.2.

240 The globally integrated scaled sensitivity is negligibly small for sufficiently short
 241 lags, in part because the scaled sensitivity field features dipoles that partially cancel each
 242 other out, but mostly because the scaled sensitivities are weaker overall for short lags
 243 (Figure 2(g)). Relative to the target year, RVP heat content is more sensitive to heat

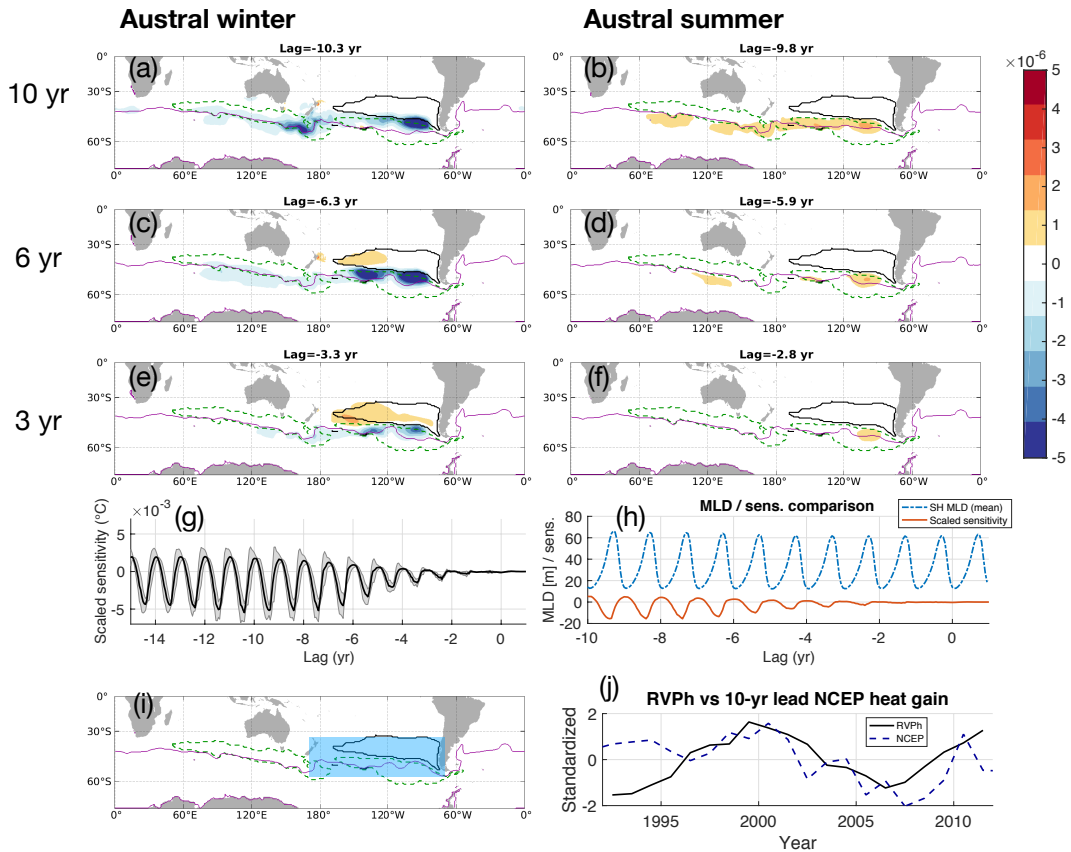


Figure 2. (a)-(f) Ensemble mean sensitivity of fixed volume RVP heat content to net heat flux, scaled by anomalies relative to annual mean climatology. At each grid cell, the eventual impact of the 14-day averaged forcing anomalies is shown in $^{\circ}\text{C}$. The seasonal cycle has not been removed from the anomalies. Positive/negative regions are associated with an eventual increase/decrease in annual mean RVP, occurring after the indicated lag timescale has elapsed. For reference, we plot the 14-day mean SAF proxy (solid blue line), a cut through the RVP at roughly 553 m depth (black solid line), and a cut through the mixed layer mask at roughly 300 m depth (green dashed line). (g) Ensemble mean (solid line) and ensemble standard deviation (shading) scaled sensitivity, where lag 0 marks the start of the target year. (h) Southern Hemisphere mean mixed layer depth (blue dot-dash line) and sensitivity (red solid line, scaled arbitrarily for visibility). (i) Blue shading indicates the area over which NCEP heat gain is integrated, and (j) shows a standardized comparison of annual mean RVP with 10-year lead heat gain from NCEP.

244 flux from previous winters than from the most recent winter. For sufficiently long lags,
 245 the globally integrated scaled sensitivities show a clear seasonal cycle, in which the scaled

246 sensitivities become more negative as the Southern Hemispheric (SH) mixed layer deep-
 247 ens (Figure 2(h)). The scaled sensitivities lead the SH mixed layer depth by roughly 1.8
 248 months ($R^2 = 0.81$), which coincides with the period of strong mixing *before* the MLD
 249 reaches its deepest value. The ensemble standard deviation is relatively small (Figure
 250 S5); the largest standard deviations are located in regions where the sensitivities them-
 251 selves are large, indicating that the sensitivity patterns are broadly coherent between en-
 252 semble members.

253 We have compared RVP_h with integrated net heat flux anomalies over the broad
 254 region (55°S-35°S, 170°E-70°W) taken from the NCEP/NCAR reanalysis (Kalnay et al.,
 255 1996) (Figure 2j). The heat flux time series has been offset in the figure such that it leads
 256 RVP_h by 10 years, and we observe a possible relationship between the two quantities over
 257 much of the period considered, indicating a decadal timescale for propagation of the anoma-
 258 lies into the RVP. Note the lack of agreement in the first 4 years of the time series may
 259 reflect uncertainties in the heat flux time series as NCEP/NCAR is poorly constrained
 260 by observations prior to commencement of the satellite era in the mid-1980s (i.e. mid-
 261 1990s when lagged by 10 years).

262 3.2 Heat flux perturbation experiments

263 In order to better understand the response of the RVP to net heat flux anomalies,
 264 we carried out four net heat flux perturbation experiments. We applied both positive
 265 and negative heat flux anomalies, with magnitude 50 W/m², over either June-July-August
 266 (JJA) or January-February-March (JFM), over a region of high linear sensitivities (Fig-
 267 ure 3). As expected from the linear sensitivities, RVP_h is more sensitive to perturbations
 268 in Austral winter (JJA) than to perturbations in Austral summer (JFM) (Figure 3b,c).
 269 A positive heat flux anomaly (ocean heat loss) cools the RVP, and a negative heat flux
 270 anomaly (ocean heat gain) eventually warms the RVP, with a lag between forcing and
 271 response. For JJA perturbations, the maximum anomaly occurs roughly three years af-
 272 ter the perturbation is applied, whereas the JFM response lacks a clear maximum.

273 This difference in timescale may reflect variations in the key processes involved. In
 274 summer, heat flux perturbations are likely dominated by solar forcing and confined to
 275 the near surface layer. The resulting temperature anomalies may not influence the RVP
 276 immediately the following winter if the winter mixing in the summer modified region is

277 weak. Overall, summertime perturbations have little influence on RVP heat content. In
 278 winter, heat flux perturbations affect the RVP via both direct heat loss and by strength-
 279 ening convection. The approximate three-year lag is likely the combined result of the ad-
 280 vection timescale into a region of strong mixing, the recurrence timescale for winters se-
 281 vere enough to produce mixing throughout the RVP, and the timescale of subduction
 282 and ventilation into the RVP.

283 Adjoint models calculate the *linear* sensitivity of an objective function. We can de-
 284 compose the response of RVPh into linear and nonlinear components (details in Appendix
 285 A). In the JFM case, the linear approximation is a good representation of the full non-
 286 linear response; by magnitude, the maximum nonlinear response is roughly 8% of the
 287 maximum linear response. For the JJA perturbations, the linear approximation is also
 288 suitable, where the maximum magnitude nonlinear response is roughly 17% of the max-
 289 imum magnitude linear response. The difference between the linear and nonlinear com-
 290 ponents may be a way to quantify the error in the adjoint approximation. The adjoint
 291 sensitivity fields cannot represent the tendency of heat fluxes to change mixing and con-
 292 vection via altering stratification. In this case, the error associated with this assump-
 293 tion is quantified by the difference between the linear and non-linear responses (Figure
 294 3). The quasi-linearity of the response indicates that the modulation of mixing by heat
 295 flux anomalies is not a major effect in terms of altering RVPh, especially considering that
 296 $50W/m^2$ is a large perturbation relative to climatological wintertime cooling.

297 **3.3 Sensitivity to zonal wind stress**

298 The scaled sensitivities, which have been convolved with zonal wind stress anoma-
 299 lies, represent the linear changes induced in RVPh by the 14-day averaged wind stress
 300 anomalies (Figure 4). Overall, Austral wintertime anomalies induce a larger linear change
 301 than Austral summertime anomalies, reflecting the seasonal cycle in the wind stress forc-
 302 ing fields rather than the comparatively weaker seasonal cycle in the underlying unscaled
 303 sensitivity fields. The sensitivity fields feature a number of dipoles, suggesting sensitiv-
 304 ity to wind-driven convergence and divergence at the surface. Broadly speaking, the dipole
 305 patterns have stronger magnitudes in Austral winter than in Austral summer, which by
 306 contrast tends to feature mostly positive scaled sensitivities (Figure 4). At 10 year lag,
 307 the scaled sensitivity pattern extends as far west as the Agulhas current retroflexion (south
 308 of South Africa) and as far south as roughly $60^\circ S$, just south of the SAF proxy. The non-

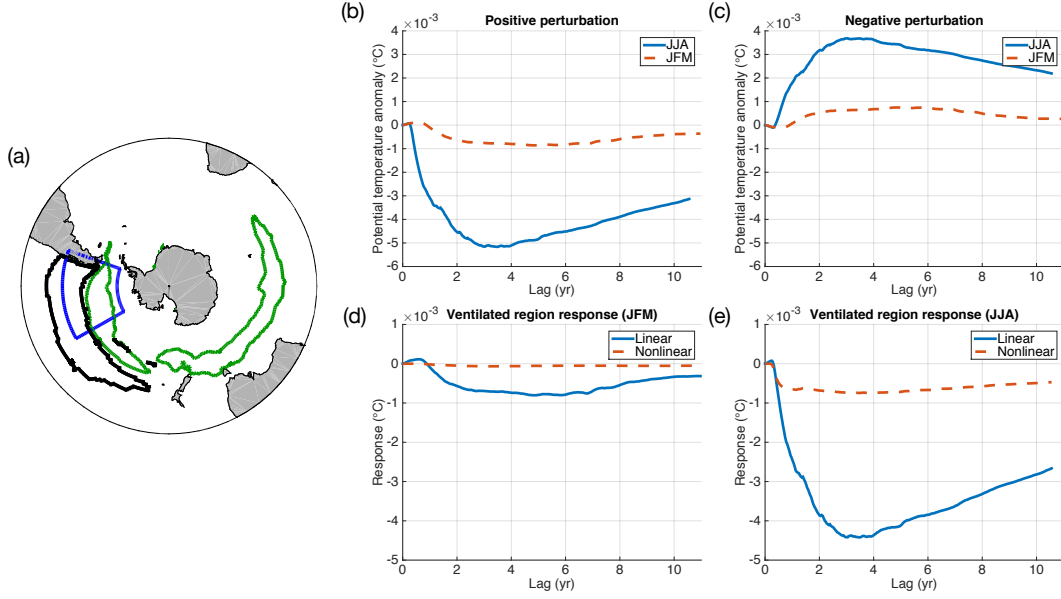


Figure 3. Net heat flux perturbation experiments. (a) Region of the imposed heat flux perturbations (blue dotted line), with the mixed layer mask (green) and ventilated region mask (black line) for reference. (b) Response of the ventilated region to a positive net heat flux perturbation, corresponding to ocean heat loss, imposed in either June-July-August (solid blue line) or January-February-March (red dashed line). (c) Same as (b), but for a negative heat flux perturbation, corresponding to ocean heat gain. (d) The linear and non-linear components of the ventilated region heat content for heat flux perturbations imposed over JFM. (e) Same as (d), except for heat flux perturbations imposed over JJA.

309 zero sensitivity values south of the SAF proxy are broadly consistent with Rintoul and
 310 England (2002), who find that Ekman transport across the South Antarctic Front (SAF)
 311 south of Australia can eventually impact the temperature properties of SAMW. Our sen-
 312 sitivity fields are also broadly consistent with Gao et al. (2018), who find wind stress curl
 313 between the SAF and the Polar Front (PF) can warm the SAMW. At shorter lags, the
 314 sensitivity field is increasingly local, suggesting that wind stress anomalies on timescales
 315 of 1-3 years and located south of the ACC have a negligible impact on RVPh.

316 The globally integrated scaled sensitivity to zonal wind stress shows a strong sea-
 317 sonal cycle for relatively short lags, but at longer lags the seasonal cycle is harder to de-
 318 tect (Figure 4(i)). This is partly due to the presence of dipoles in the scaled sensitivity
 319 fields, which cancel out when added together. The integrated scaled sensitivity is roughly
 320 anti-correlated with SH mixed layer depth, with MLD leading sensitivity by less than

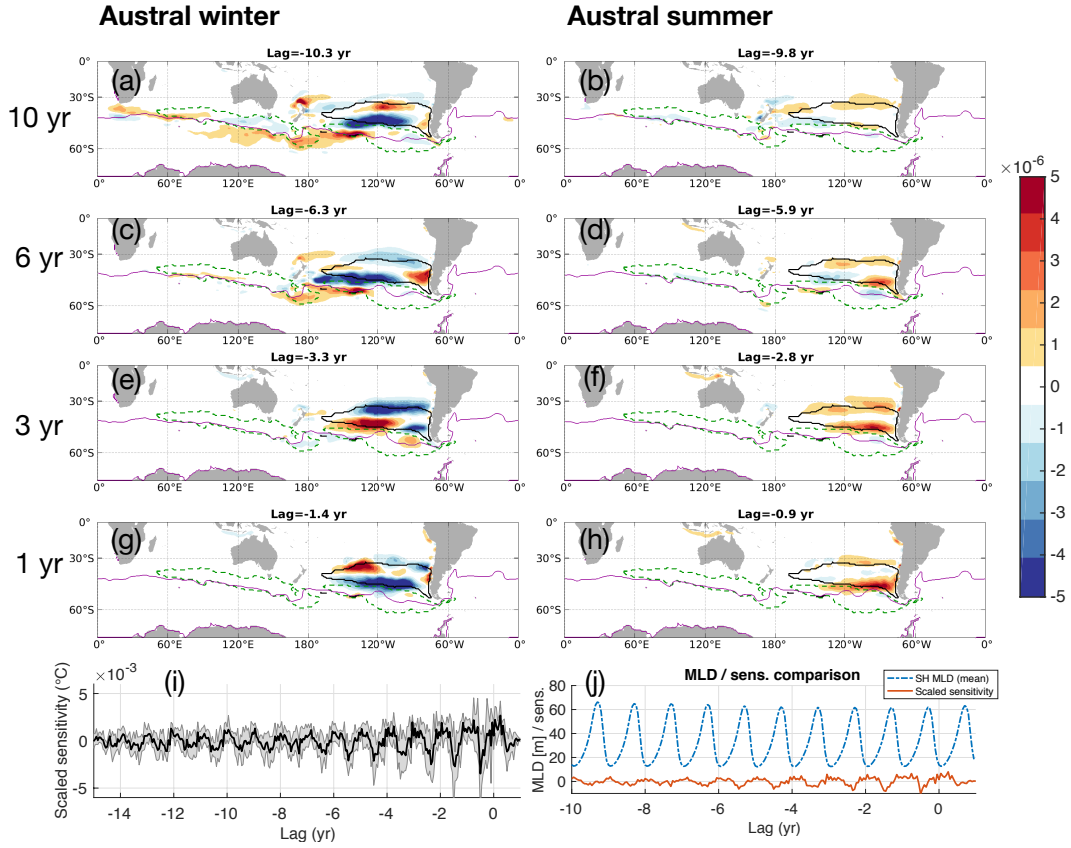


Figure 4. (a)-(f) Ensemble mean sensitivity of fixed volume RVP heat content to zonal wind stress, scaled by anomalies relative to annual mean climatology. At each grid cell, the eventual impact of the 14-day averaged forcing anomalies is shown in $^{\circ}C$. The seasonal cycle has not been removed from the anomalies. Positive/negative regions are associated with an eventual increase/decrease in annual mean RVP, occurring after the indicated lag timescale has elapsed. We show a set of 14-day means at selected lags. For reference, we plot the 14-day mean SAF proxy (solid blue line), a cut through the objective function volume at roughly 553 m depth (black solid line), and a cut through the mixed layer mask at roughly 300 m depth (green dashed line). Units are degrees C. (g) Time series of ensemble mean (solid) and ensemble standard deviation (shading) scaled sensitivity.

321 one month ($R^2 = 0.36$). The scaled sensitivity becomes more negative as the mixed layer
 322 deepens. The lag correlation between MLD and scaled sensitivity is periodic, with a pe-
 323 riod of approximately one year and little change in amplitude, indicating a strong cor-
 324 relation between the seasonal cycles of MLD and the scaled sensitivity.

325 The unscaled sensitivity to zonal wind stress ($\partial J/\partial \tau_e$) features a persistent dipole
 326 pattern that spatially coincides with the RVP, with positive sensitivities in the south-
 327 ern part and negative sensitivities in the northern part (Figure S3). If one were to per-
 328 turb the zonal wind stress using a pattern with the same sign and spatial distribution
 329 as the sensitivities, one would induce gyre-scale Ekman convergence and Ekman pump-
 330 ing, thereby pushing isopycnal surfaces associated with the subtropical gyre downward.
 331 The resulting combination of isopycnal heave and the spinup of the subtropical gyre would
 332 increase RVPh.

333 3.4 Zonal wind stress step response experiments

334 The scaled sensitivity fields suggest that, on the 0-15 year timescales considered
 335 in this work, RVPh is most sensitive to local wind stress anomalies, specifically those that
 336 spatially coincide with the latitude-longitude range of the RVP and with the eastern por-
 337 tion of the South Pacific subpolar gyre. The RVP is also sensitive to wind stress anoma-
 338 lies in the mode water formation and subduction region found in the Eastern Pacific. Fur-
 339 thermore, on timescales longer than 5-6 years, the RVP is also sensitive to wind stress
 340 anomalies south of the SAF proxy. In order to examine the adjustment of the RVP to
 341 anomalies in these three broad regions, we performed three pairs of wind stress step re-
 342 sponse experiments, using three different spatial patterns and signs that either match
 343 the sensitivity fields (called the “positive” experiments) or oppose them (called the “neg-
 344 ative” experiments, in that they have been multiplied by -1) (Figure 5). All step changes
 345 have the same magnitude of 0.020 N/m^2 , which is roughly 22% of the 1992-2011 mean
 346 zonal wind stress between 30°S and 70°S (0.090 N/m^2) and roughly 80% of the standard
 347 deviation averaged over the same latitudes (0.025 N/m^2). All perturbations start in model
 348 year 1996; we chose this year as the stratification before 1996 is anomalously weak rel-
 349 ative to the 1992-2011 mean.

350 The “gyre” forcing pattern (Figure 5a) is derived from the unscaled sensitivities
 351 (Figure S3). This pattern represents the influence of wind stress curl on spinning up or
 352 spinning down the gyre, with the associated shifts on isopycnal depths. Based on the un-
 353 scaled sensitivities, uniform perturbations in this area are expected to have the largest
 354 impact on RVP heat content than any other region. The “subduction” forcing pattern
 355 (Figure 5b) is over a region where there are deep mixed layers which is also part of the
 356 ventilated region - changes in wind forcing here may affect the rate of water mass sub-

357 reduction into the ocean interior. Based on the unscaled sensitivities, uniform perturba-
 358 tions in this area will have a smaller but non-zero effect on the heat content of the RVP.
 359 Finally, the “high latitude” forcing pattern (Figure 5c) is south of the SAF proxy, i.e.
 360 in a region largely dominated by circumpolar flow. Wind stress changes here can affect
 361 the high-latitude upwelling which forms a crucial part of the overturning circulation. Based
 362 on the unscaled sensitivities, this region is expected to have a relatively small effect on
 363 the heat content of the RVP.

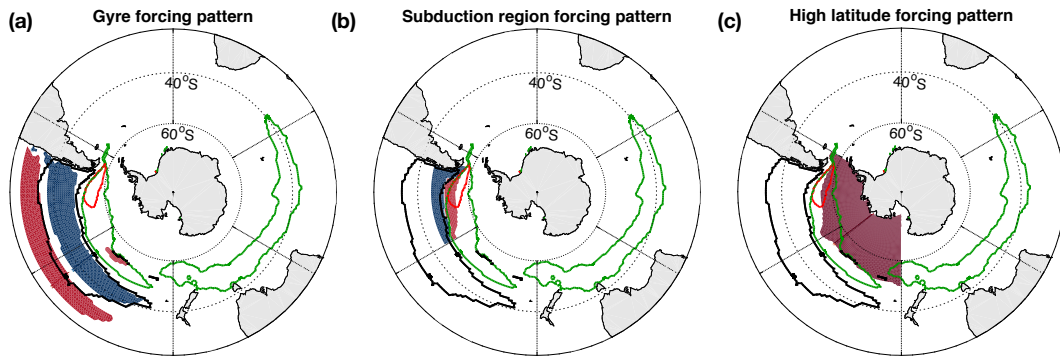


Figure 5. Zonal wind stress step response experiment types, namely (a) gyre forcing, (b) forcing over the subduction region, and (c) high-latitude forcing. Positive (red) regions indicate eastward wind stress, and negative (blue) regions indicate westward wind stress. This plot shows the perturbations that are referred to as positive. Shown for reference is the mixed layer mask (green), the ventilated region mask (black), and a 600 m maximum mixed layer contour (red). The perturbation fields referred to as “negative” have the opposite signs of those shown.

364 The impacts of the step changes in wind stress agree well with the impacts sug-
 365 gested by the scaled sensitivity fields (Figure 6). In response to the positive gyre step
 366 change, the RVP warms roughly linearly at a rate of 0.09 °C/decade. In response to the
 367 positive subduction region step change, the RVP warms roughly linearly at a rate of 0.04
 368 °C/decade, and in response to the high-latitude change, the RVP warmed at a rate of
 369 0.02 °C/decade. In response to the negative perturbations, the RVP cools in all three
 370 cases, albeit at weaker rates than in the positive step change cases; the cooling induced
 371 by the high latitude and subduction patterns is nearly identical (Figure 6b). For all three
 372 patterns, the responses are largely linear across all timescales considered here (0-12 years)
 373 (Figure 6c). After 12 years, the response to the gyre pattern is 79% linear, the response
 374 to the high latitude pattern is 99% linear, and the response to the subduction pattern

375 is 69% linear. The warming induced by the positive step changes roughly match those
 376 predicted by the adjoint sensitivities, calculated by convolving the unscaled adjoint sensi-
 377 tivity fields with the imposed step change patterns (Figure 6d-f). The differences be-
 378 tween the responses in the non-linear forward experiment and the responses predicted
 379 by the linear adjoint sensitivity fields highlight differences between the forward and ad-
 380 joint model, specifically the absence of non-linear processes in the adjoint.

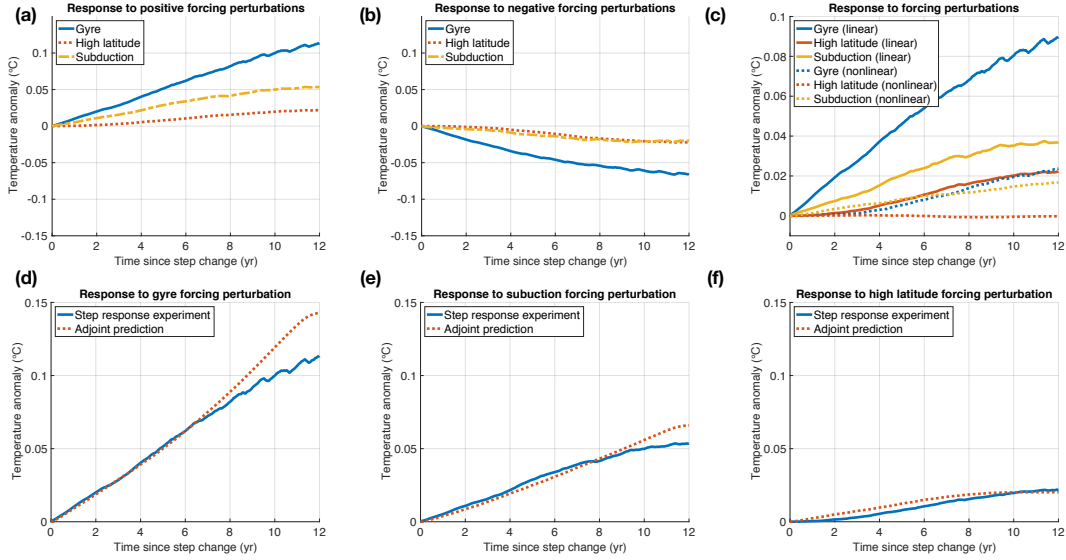


Figure 6. Response of the (fixed volume) RVP defined in the text to (a) the positive forcing patterns and (b) the negative forcing patterns. All three experiment types are shown; gyre (blue solid lines), high latitude (red dotted lines), and subduction (green dash-dot lines). (c) The linear (solid lines) and nonlinear (dotted lines) responses to the three different forcing patterns. Also shown are comparisons between the results of the step response experiment and the change predicted by convolving the adjoint sensitivity fields with the imposed change in wind stress for the (d) gyre, (e) subduction, and (f) high latitude forcing patterns.

381 Although the imposed changes in wind stress are relatively simple, the responses
 382 that they induce can be complex. In order to analyze the response mechanisms excited
 383 by the imposed step changes in wind stress, we examine sections of annual mean tem-
 384 perature anomalies in the far eastern South Pacific (Figure 7). The negative gyre forc-
 385 ing induces Ekman suction (upwelling) centered at roughly 37°S and the associated shoal-
 386 ing of interior isopycnals, bringing relatively cold water from below into the fixed vol-
 387 ume RVP, thereby reducing the RVP_h as seen in Figure 6b. The negative gyre forcing

388 also induces warming at lower latitudes, but this does not directly affect RVP. The oppositely-
 389 signed positive gyre forcing mostly induces the opposite pattern, i.e. Ekman pumping,
 390 downwelling between 30-40°S, and deepening of isopycnals that moves relatively warm
 391 water into the fixed volume RVP.

392 The high latitude forcing perturbation has only a weak impact on the positions of
 393 the isopycnals that cut through the RVP, instead inducing changes in the water that subducts
 394 into the RVP. The negative perturbation moves cold, high-latitude water northwards across
 395 the ACC via Ekman transport, where cold anomalies can then be subducted below the
 396 mixed layer and into the RVP. The positive perturbation induces the opposite response,
 397 with poleward Ekman transport anomalies leading to an anomalously warm RVP.

398 The subduction forcing perturbation changes high-latitude wind stress curl and the
 399 associated Ekman suction/pumping, which leads to shoaling/deepening of isopycnals be-
 400 tween 40-50°S and cooling/warming of the RVP. The perturbation also induces warm-
 401 ing/cooling of the water that subducts into the RVP that resembles a combination of
 402 the patterns induced by the high latitude change and gyre change, albeit on deeper isopy-
 403 cnals. The responses within the RVP due to Ekman changes and the responses in the
 404 RVP source waters have opposite signs, so the net effect depends on the balance between
 405 isopycnal heave and changes in properties of the subducted water.

406 **3.5 Sensitivity to northward wind stress**

407 The meridional wind stress sensitivity fields indicate that the RVP is sensitive to
 408 wind stress along the west coast of South America and, on timescales longer than 4-5
 409 years, to wind stress along the west coast of New Zealand in winter (Figure 8). North-
 410 ward wind stress parallel to the western coast of Chile induces Ekman transport away
 411 from the coast, creating cross-shelf pressure gradients and anomalous upwelling. South-
 412 ward wind stress has the opposite effect, ultimately suppressing coastal upwelling. The
 413 unscaled sensitivity fields show consistently positive sensitivities along much of the Chilean
 414 coast, with negative along-coast sensitivities to the north, and positive offshore sensi-
 415 tivities (Figure S4). The unscaled sensitivities do not change significantly with season,
 416 but the scaled sensitivities, which have been convolved with northwards wind stress anoma-
 417 lies, show a seasonal cycle. The scaled sensitivities along the Chilean coast are negative
 418 in Austral winter and positive in Austral summer. In combination with the unscaled sen-

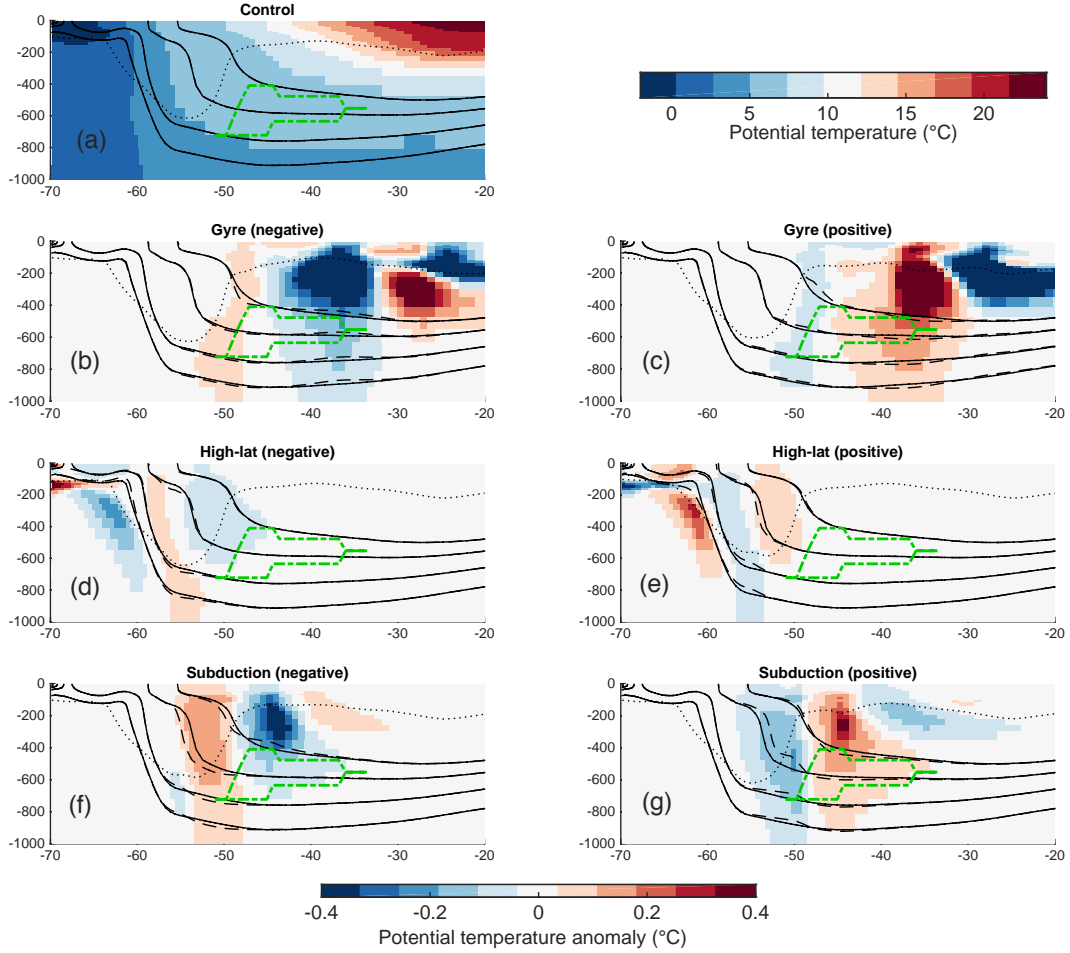


Figure 7. Response of potential temperature and density to step changes in wind stress, shown as annual mean potential temperature anomaly sections at 100°W , relative to the control run [shown in panel (a)], 10 years after the step change in zonal wind stress. In each panel, we plot a cut through the (fixed volume) RVP used in the adjoint sensitivity experiments (green dash-dot line), the maximum mixed layer depth (black dotted line), annual mean potential density surfaces (indicating $26.9\sigma_0$ to $27.2\sigma_0$, in 0.1 kg/m^3 increments) for the control run (solid black lines) and the step response experiments (dashed black lines). We plot anomalies for the gyre forcing pattern (b,c), the high-latitude forcing pattern (d,e), and the subducted region forcing pattern (f,g).

419 sensitivity fields, this indicates that in winter, southward meridional wind stress anomalies
 420 suppress coastal upwelling, linked with a drop in RVP, and in summer northward anomalies
 421 increase upwelling, linked with a rise in RVP. The mechanisms are investigated in
 422 the perturbation experiments in section 3.6.

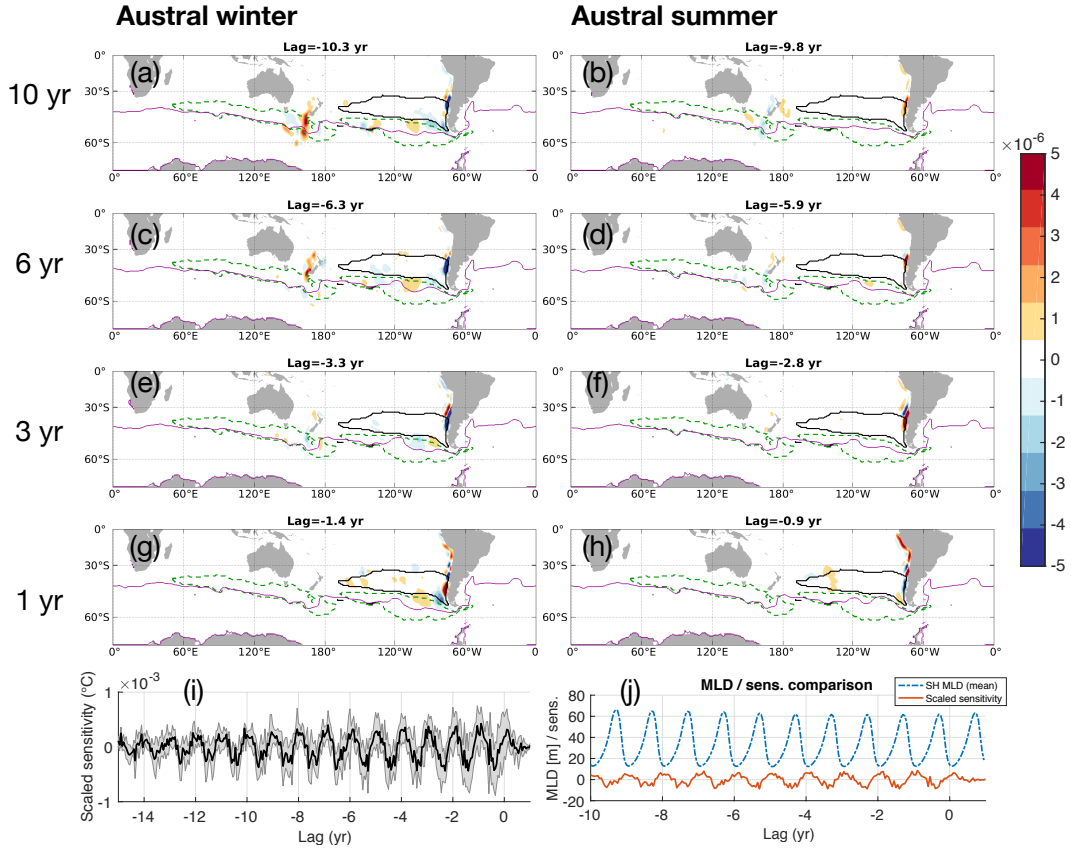


Figure 8. (a)-(d) Ensemble mean sensitivity of fixed volume RVP heat content to meridional wind stress, scaled by anomalies relative to annual mean climatology. At each grid cell, the eventual impact of the 14-day averaged forcing anomalies is shown in $^{\circ}C$. The seasonal cycle has not been removed from the anomalies. Positive/negative regions are associated with an eventual increase/decrease in annual mean RVP ϕ , occurring after the indicated lag timescale has elapsed. For reference, we plot the 14-day mean SAF proxy (solid blue line), a cut through the objective function volume at roughly 553 m depth (black solid line), and a cut through the mixed layer mask at roughly 300 m depth (green dashed line). (e) Time series of ensemble mean (solid) and ensemble standard deviation (shading) scaled sensitivity.

423 The globally integrated scaled sensitivity shows a seasonal cycle in both the ensemble
 424 ble mean and standard deviation (Figure 8(i)). Southern Hemisphere MLD leads the scaled
 425 sensitivity by roughly one month ($R^2 = 0.49$). The scaled sensitivity gets more nega-
 426 tive as the mixed layer deepens, and the scaled sensitivity gets more positive as the mixed
 427 layer shoals [Figure 8(j)]. The lag correlation between the meridional wind stress and
 428 the mixed layer is periodic, with a period of approximately one year and little change

429 in magnitude, indicating a persistent correlation between the seasonal cycles of both quan-
 430 tities. The overall magnitude of the scaled sensitivity is weaker than that of zonal wind
 431 stress, in part due to the smaller area occupied by the meridional sensitivity fields.

432 **3.6 Meridional wind stress step response experiments**

433 To investigate adjustment mechanisms highlighted by the scaled sensitivities, we
 434 performed a pair of meridional wind stress step response experiments. We imposed the
 435 step change along the western coast of Chile (Figure 9a), either northwards or southwards
 436 with a magnitude of 0.02 N/m^2 . This is a relatively large perturbation compared with
 437 the mean meridional wind stress (magnitude 0.008 N/m^2) and larger than the spatial-
 438 mean standard deviation (0.01 N/m^2), calculated between 60°W - 80°W and 30°S - 70°S .
 439 The northward wind stress anomaly induces Ekman transport away from the coast, cre-
 440 ating a negative pressure anomaly that rapidly propagates around the southern tip of
 441 South America (Figure 9b). The associated coastal upwelling brings cooler waters up
 442 to the surface, creating negative SST anomalies (Figure 9c). The change in pressure even-
 443 tually changes the barotropic circulation identified with the subtropical gyre and the ACC.
 444 The resulting change in circulation alters the heat convergence into the RVP and induces
 445 warming (Figure 9e). The negative step response experiment produces the opposite re-
 446 sponse; indeed, the response of the RVP to this set of step response experiments is al-
 447 most entirely linear (Figure 9f).

448 **3.7 Comparing scaled sensitivities net heat flux and wind stress**

449 For lags shorter than 3-5 years, RVP ϕ is most sensitive to globally-integrated wind
 450 stress anomalies relative to annual mean climatology, and for longer lags, RVP ϕ is most
 451 sensitive to globally-integrated net heat flux anomalies [Figure 10(a)]. Wind stress anoma-
 452 lies can directly alter RVP ϕ by inducing wind stress curl anomalies over the RVP, which
 453 drives isopycnal heave. Net heat flux anomalies take longer to affect RVP ϕ because these
 454 anomalies must ultimately propagate from the surface into the RVP following subduc-
 455 tion pathways. Both scaled sensitivity time series feature a strong seasonal cycle, indi-
 456 cating a coupling with mixed layer dynamics as discussed in previous sections.

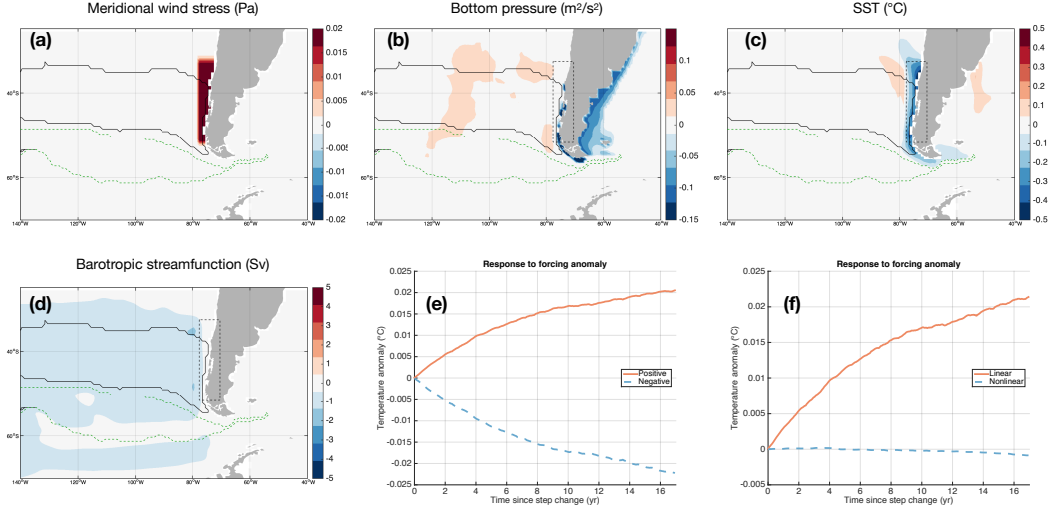


Figure 9. (a) Imposed meridional wind stress perturbation, along with mixed layer mask (green dashed line) and the RVP mask (black solid line) for reference. Annual mean anomalies for the (b) bottom pressure, (c) sea surface temperature, and (d) barotropic streamfunction are shown, 10 years after the imposed wind stress anomaly. Also shown is the time series of (e) the RVP response to positive and negative imposed anomalies and (f) the linear and nonlinear components of this response.

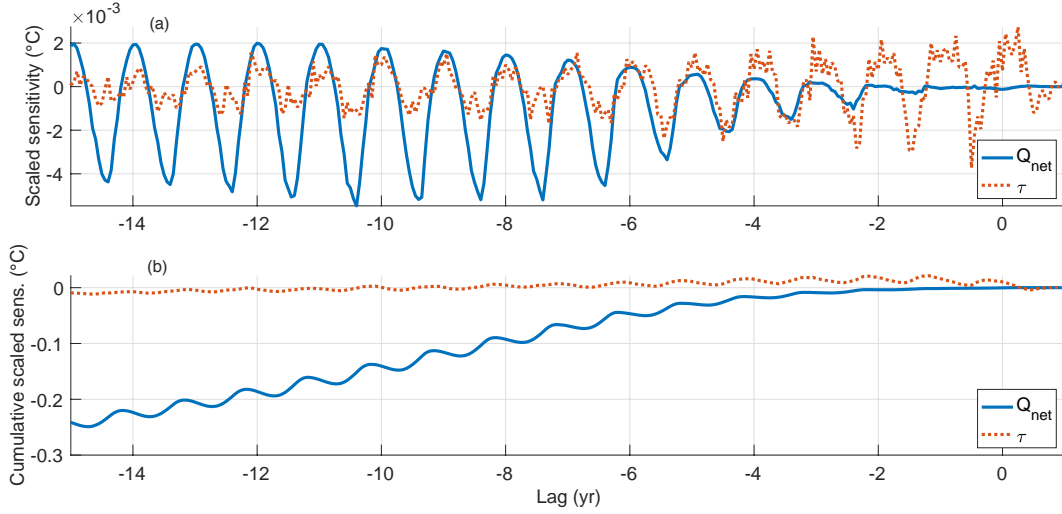


Figure 10. Time series of (top) scaled sensitivity and (bottom) cumulative scaled sensitivity. Here we combine the linear impacts of zonal wind stress and meridional wind stress into a single “wind stress” measure.

457

The cumulative effects of surface forcing anomalies on RVP are estimated as fol-

458

lows:

$$dJ_{cumulative,x}(t) = \int_A \int_{t'=t}^{1yr} \Delta J(\mathbf{r}, t') dt' dA = \int_A \int_{t'=t}^{1yr} \left[\frac{\partial J}{\partial x}(\mathbf{r}, t) \right] [x(\mathbf{r}, t) - \bar{x}(\mathbf{r})] dt' dA, \quad (3)$$

459 where x is one of the surface forcing variables (i.e. net heat flux, zonal wind stress, merid-
 460 ional wind stress). We integrate over the global ocean area A , from time t throughout
 461 the entire target year (to $t' = 1$ yr). The cumulative impact of wind stress anomalies
 462 is ultimately close to zero, as the warming and cooling impacts roughly cancel out on
 463 sufficiently long timescales, leaving only a small residual [Figure 10(b)]. Reading the fig-
 464 ure from right to left, the cumulative effect of net heat flux perturbations is a long-term
 465 cooling, reflecting the collective action of anomalies over an increasing fraction of ocean
 466 surface area with time and also the predominance of wintertime heat flux anomalies. By
 467 comparison, wind stress terms roughly cancel out when averaged over a seasonal cycle.

468 RVP_h is most sensitive to surface forcing anomalies (relative to annual mean cli-
 469 matology) integrated over the Pacific basin [Figure 11(a,b)]. This is not surprising, as
 470 the RVP is situated in the relatively isolated far eastern Pacific Ocean. Note the asym-
 471 metry about zero in the Pacific time series (Figure 11(a), which explains a large frac-
 472 tion of the asymmetry about zero in Figure 10. Net heat flux anomalies in the Indian
 473 basin make a significant contribution as well, largely driven by anomalies south of Aus-
 474 tralia and New Zealand. Wind stress sensitivity is especially dominated by anomalies
 475 in the Pacific basin, mostly reflecting the impact of the local wind stress curl. We find
 476 that RVP_h is most sensitive to surface forcing anomalies north of the SAF proxy [Fig-
 477 ure 11(c,d)], although heat flux anomalies south of the SAF proxy do increase with lag.
 478 Overall, surface forcing anomalies in regions south of the SAF proxy do not have a strong
 479 impact on the fixed-volume RVP_h.

480 **4 Discussion of interannual variability, changes in the ventilated vol-** 481 **ume, and on forcing versus interior changes**

482 Regional variations in surface forcing across a wide range of timescales can ulti-
 483 mately impact the Southern Ocean subduction and ventilation process, which forms a
 484 critical part of the meridional overturning circulation (MOC) (Marshall & Speer, 2012b).
 485 The transport of heat and carbon by the MOC critically affects the partition of heat and
 486 carbon between the ocean and the atmosphere, regulating the rate of anthropogenic sur-
 487 face warming. We used a suite of adjoint sensitivity experiments to highlight the spe-
 488 cific locations and timescales on which ocean properties, net heat flux, and wind stress
 489 can affect the heat content of the recently ventilated interior. We focused our attention
 490 on an especially efficient export pathway, which carries weakly stratified water from the

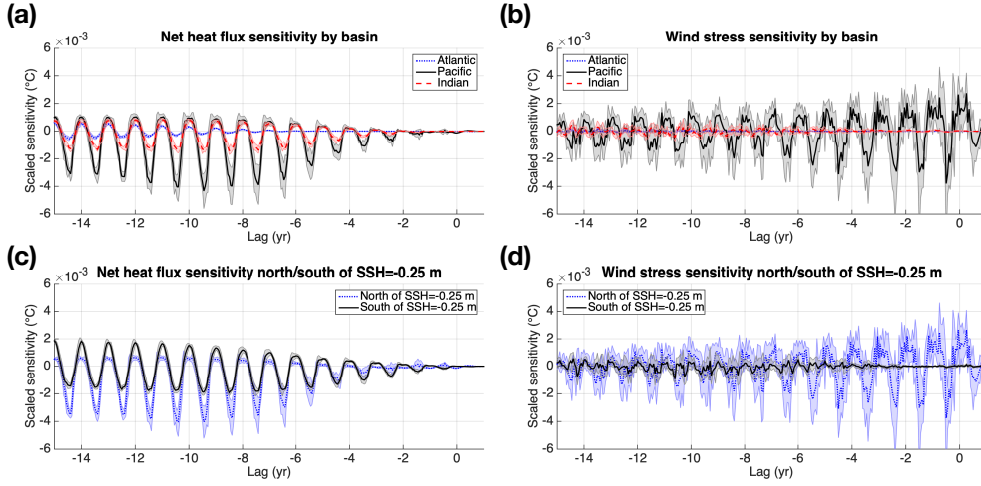


Figure 11. Scaled sensitivity time series for net heat flux and wind stress, decomposed by (a,b) ocean basin and (c,d) position north or south of the SAF proxy. Zonal and meridional wind stresses have been combined into a single wind stress measure.

491 surface into the interior Pacific. An extension of this work into multiple basins would
 492 be a welcome addition to this study.

493 4.1 Interannual variability in surface forcing

494 In order to highlight the locations and timescales where interannual surface forc-
 495 ing most contributes to variability in annual mean RVPh, we present an alternative set
 496 of scaled sensitivities that have been convolved with monthly mean forcing anomalies,
 497 highlighting departures from the ECCO seasonal cycle:

$$\Delta J(\mathbf{r}, t) = \left[\frac{\partial J}{\partial x}(\mathbf{r}, t) \right] [x(\mathbf{r}, t) - \bar{x}(\mathbf{r}, t)], \quad (4)$$

498 where \bar{x} is the monthly mean climatology of the forcing field over 1992-2011. First and
 499 foremost, the magnitudes are reduced as one would expect since the relatively large and
 500 persistent seasonal signal has been omitted. The overall spatial patterns of sensitivity
 501 are similar to those derived using anomalies from annual mean climatology, with some
 502 notable differences (Figure 12). In the Pacific sector, RVPh is most affected by net heat
 503 flux anomalies south of the RVP projection and north of the SAF proxy, which lies within
 504 a region of deep mixed layers, and in the Indian sector, we find regions of sensitivity south
 505 of the SAF proxy. The locations of these sensitivities are consistent with those from an-
 506 nual mean climatology (Figure 2) and with the unscaled sensitivity (see supporting info),

507 but the sign structure is more complex, reflecting departures from monthly mean forc-
 508 ing values. We find similar results with both zonal and meridional wind stress. The globally-
 509 integrated sensitivity values are much smaller than in the climatological case, reflecting
 510 the increased presence of sensitivity dipoles that cancel out during integration (Figure
 511 S8).

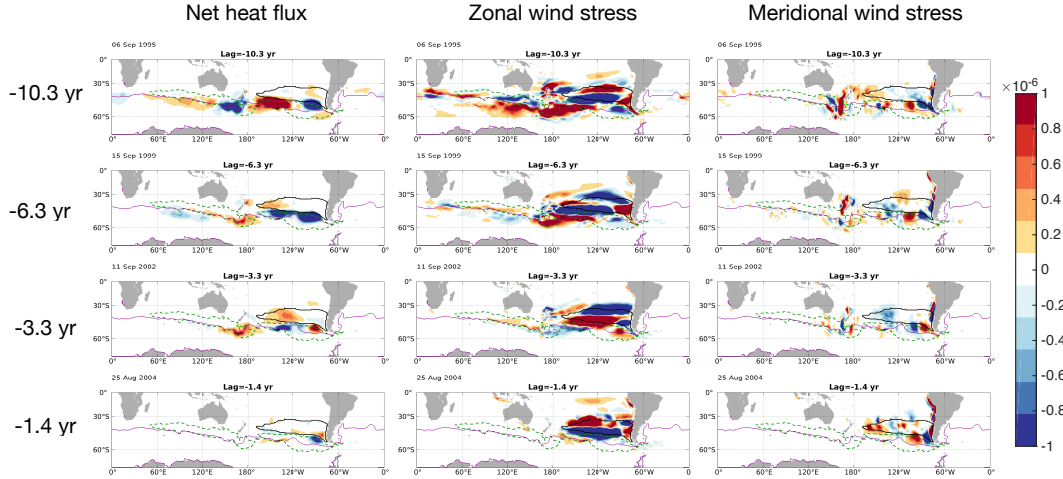


Figure 12. Ensemble mean sensitivity of fixed volume RVP heat content to surface forcing components, scaled by anomalies relative to monthly mean climatology (i.e. monthly mean values have been subtracted from the forcing fields). At each grid cell, the eventual impact of the 14-day averaged forcing anomalies is shown in $^{\circ}C$. Positive/negative regions are associated with an eventual increase/decrease in annual mean RVP heat content, occurring after the indicated lag timescale has elapsed. Each plot shows a 14-day mean taken sometime in Aug-Sep, i.e. Austral winter. Note that that the color scale is different than for previous scaled sensitivity plots.

512 **4.2 Changes in the ventilated volume**

513 We found that on timescales shorter than roughly 4-6 years, RVP heat content is strongly af-
 514 fected by wind stress anomalies above the SPG. Wind stress curl anomalies over the SPG
 515 affect Ekman convergence/divergence and the associated Ekman pumping/suction that
 516 drives isopycnal heave. The relative dominance of the SPG in setting RVP heat content may seem
 517 at odds with the canonical view of the MOC in the Southern Ocean (Marshall & Speer,
 518 2012b). In this view, Circumpolar Deep Water is upwelled south of the ACC as part of
 519 the residual overturning circulation and exported northwards at the surface, getting mod-
 520 ified by surface fluxes, and ultimately being subducted as SAMW and AAIW where it

521 spreads along isopycnals into the subtropical gyres. Changes in the properties of this sub-
 522 ducted volume are then thought to be more sensitive to changes in the subducted wa-
 523 ter masses and their southern sources (Garabato et al., 2009; Cerovecki et al., 2019, e.g.)
 524 and thus it is surprising to see the weak sensitivity fields over the ACC relative to the
 525 subtropical gyre. The difference can be understood due to the fixed volume nature of
 526 the RVP as defined in the adjoint model. Here we must use a fixed volume based on the
 527 model setup, which captures the mean position of the ventilated water but does not move
 528 with the isopycnals as they heave. The RVP is therefore not strictly analogous to SAMW.
 529 Deepening of the thermocline driven by heave in the subtropical gyre will significantly
 530 impact the RVP, while potentially not actually changing the heat content of recently sub-
 531 ducted SAMW (defined between two isopycnals) at all. We must be careful not to con-
 532 flate the RVP as defined here with the upper limb of the overturning circulation. How-
 533 ever, this is not to say that this analysis tells us nothing about subduction. Gao et al.
 534 (2018) for example show that the majority of recent heat uptake by SAMW is driven not
 535 by a change in the SAMW properties, but instead by a thickening of the layer, largely
 536 driven by changes in wind forcing and subduction in the regions of deep mixed layers.
 537 This aligns well with the findings in the forward runs (Figure 11) where the subduction
 538 experiment over the SAMW formation regions is more impactful on RVP heat content
 539 than the high latitude experiment. Further analysis of this distinction in the adjoint of
 540 a model defined on isopycnal surfaces would be revealing and we may expect to see a weaker
 541 response to fluxes over the subtropical gyre, but is beyond the scope of the present work.

542 Although changes in isopycnal layer thickness are not represented in the adjoint
 543 sensitivity fields, they are of course present in the “forward” step response experiments.
 544 As expected, all three “positive” step response forcing patterns induce warming on a rep-
 545 resentative interior isopycnal, with the warming being most widespread for the gyre forc-
 546 ing pattern (Figure 13[a,b,c]). However, the changes in layer thickness between $26.9\sigma_0$
 547 and $27.2\sigma_0$ are complex and regional. The gyre forcing pattern induces a thin band of
 548 concentrated thickening along the southern boundary of the RVP and a less concentrated
 549 thinning on the northern boundary of the RVP, due in part to asymmetries in the deep-
 550 ening and shoaling of isopycnals across the RVP (Figure 13[d]). The high-latitude forc-
 551 ing pattern induces mild layer thickening along the southern boundary of the RVP that
 552 largely comes from the shoaling of the $26.9\sigma_0$ isopycnal (Figure 13[e]). Finally, the “sub-

553 reduction” pattern induces thickening along the southern boundary of the RVP and thin-
 554 ning over a large fraction of the interior RVP (Figure 13[f]).

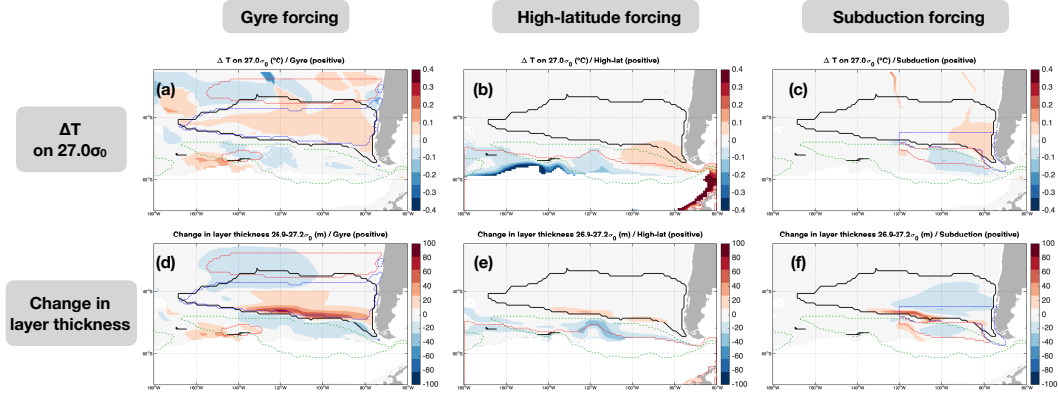


Figure 13. Annual mean changes in temperature on density levels (a-c) and changes in layer thickness (e-f), 10 years after the imposed step changes in wind stress. Blue and red contours show regions where the wind stress changes are imposed, with positive changes shown in red and negative changes shown in blue.

555 **4.3 On separating the effect of forcing changes from interior changes**

556 Consider the heat content between two isopycnal surfaces. We will call the time-
 557 varying volume between those isopycnal surfaces as the “control volume” and the heat
 558 content in the control volume as H . In the context of ventilation, any attempts to un-
 559 ambiguously disentangle heat content changes (ΔH) into components associated with
 560 (1) variations in the volume of isopycnals from those associated with (2) variations in
 561 the temperature properties between those isopycnals are fraught with conceptual diffi-
 562 culties. For example, one could repeat the passive tracer ventilation experiments using
 563 wind stress forcing patterns from each of the step response experiments used in this manuscript.
 564 The volume ventilated by the tracer will change with surface forcing; some new areas
 565 will be ventilated, and some previously ventilated areas will be in the unventilated “shadow
 566 zone”. Is it appropriate to include the heat content of the newly ventilated region in ΔH ?

567 The additional heat from an expanded ventilated volume does not necessarily come
 568 from the surface; this heat is now in the control volume thanks to altered advection path-
 569 ways and perturbed patterns of diapycnal mixing, much of which happens entirely away
 570 from the surface. If one is after a measure of ΔH that separates the direct effect of sur-

571 face forcing changes from the effect of altered advection and mixing, then including the
572 newly ventilated region in ΔH is problematic. But excluding the newly ventilated re-
573 gion from ΔH is perhaps equally problematic, as it is indeed the change in surface forc-
574 ing which altered the pattern of ventilation. In attempting to separate surface effects from
575 interior effects in the context of ventilation, we have created an over-constrained anal-
576 ysis problem.

577 If we drop the need to separate surface effects from interior changes, then the prob-
578 lem becomes much simpler. One can simply use the various passive tracer experiments
579 to define ventilated regions, and separating ΔH associated with the change in ventilated
580 volume from ΔH associated with a change in temperature within the ventilated region
581 becomes more tractable. In this case, one can associate temperature changes in the “com-
582 mon” ventilated region, i.e. the ocean volume which is ventilated in both the “control”
583 ventilation experiment and the “perturbed” ventilation experiment, with changes in ven-
584 tilated water properties, which is cleanly separate from ΔH associated with volume changes.
585 This approach is well-defined and defensible, but it does not allow one to associate changes
586 in surface forcing (e.g. a given heat flux anomaly) with separate changes in isopycnal thick-
587 ness and along-isopycnal properties. To solve this problem, we need a new conceptual
588 and modelling framework.

589 **4.4 Ocean-only models underestimate heat flux sensitivities**

590 ECCOv4-r2 is based on an instance of MITgcm in ocean-only mode. In this ECCOv4-
591 r2 setup, the 2m air temperature, 2m specific humidity, downward shortwave radiation,
592 and downward longwave radiation are specified as time-evolving boundary conditions.
593 These atmospheric variables are inputs in the bulk formulae, which use differences be-
594 tween the fixed, specified atmospheric variables and the dynamically evolving surface ocean
595 state to determine the rates of air-sea heat exchange. One consequence of this arrange-
596 ment is that the sea surface temperature tends to be overly sensitive to changes in sur-
597 face heat flux anomalies (Hyder et al., 2018). This heightened sensitivity arises from the
598 fact that while the air-sea fluxes can respond to a change in ocean surface temperature,
599 the atmospheric variables, e.g. the given values of humidity and downward radiative fluxes,
600 cannot.

601 To better understand this, consider the imposition of an arbitrary air-sea heat flux
602 perturbation. This perturbation will create a sea surface temperature anomaly that will
603 affect the exchange of heat between the surface ocean and the atmosphere. In a coupled
604 system, the SST and the atmospheric temperature will both adjust towards each other,
605 minimizing the air-sea temperature difference as heat is exchanged between the surface
606 ocean and the atmosphere. However, in an ocean-only simulation like ECCOv4-r2, only
607 the SST can adjust to the heat flux anomaly. The atmospheric variables retain their fixed
608 values, which leads to air-sea temperature differences that are initially larger than those
609 found in coupled models. Because the air-sea heat fluxes in the bulk formulae are pro-
610 portional to the air-sea temperature differences, larger air-sea temperature differences
611 lead to larger heat fluxes. By this mechanism, sea surface temperature anomalies are quickly
612 damped out by strong air-sea heat fluxes - the sea surface temperature is strongly tied
613 to the prescribed atmospheric temperature.

614 For a given flux perturbation (or forcing error) the T signal is > 5 times smaller
615 for an ocean-only model than for a coupled model (Hyder et al., 2018). So our sensitiv-
616 ities may be under-estimates relative to the full coupled system. However, this bias mainly
617 occurs at the surface, and it mainly occurs outside of the region of the perturbation. Once
618 the anomalously warm/cool water comes into contact with the atmosphere away from
619 the forcing perturbation, the anomaly can be rapidly damped away. It should not affect
620 sensitivities to interior anomalies (like the interior portions of the kinematic and dynamic
621 sensitivity fields).

622 **5 Conclusions**

623 We have used an observationally-constrained adjoint model to identify the loca-
624 tions and timescales on which surface forcing can have the largest impact on the heat
625 distribution in the recently ventilated eastern Pacific sector of the Southern Ocean. Specif-
626 ically, we find that the heat content of the fixed control volume (RVPh) is strongly af-
627 fected by forcing and properties associated with the eastern South Pacific Gyre. On timescales
628 shorter than 3-5 years, RVPh is most sensitive to wind stress anomalies that lie roughly
629 on the borders of the RVP footprint, as Ekman transport can induce Ekman pumping/suction
630 and thereby produce isopycnal heave that moves heat into and out of the fixed-volume
631 RVP. In addition, changes in large-scale gyre circulation can change heat convergence
632 in the RVP through variations in the barotropic gyre circulation. On timescales longer

633 than 3-5 years, RVPPh is strongly affected by upstream heat flux anomalies. In the Pa-
 634 cific sector, these scaled sensitivities tend to be located south of the RVP projection and
 635 north of the SAF proxy, but still in the region of deep mixed layers. In the Indian sec-
 636 tor, these scaled sensitivities can be found south of the SAF proxy, indicating the pos-
 637 sible location of cross-frontal transport that can ultimately impact RVPPh.

638 Based on the scaled and unscaled sensitivity fields (see supporting info), we can
 639 recommend locations for optimal perturbation experiments in numerical models, includ-
 640 ing higher-resolution cases, that should produce especially large variations in RVPPh re-
 641 lative to perturbations in other regions (Figure 14). In particular, we suggest that wind
 642 stress anomalies be applied at (1) the boundaries of the surface projection of the RVPPh,
 643 including along the west coast of South America, (2) along the west coast of New Zealand,
 644 or (3) south of the SAF (or a suitable proxy) in the Indian sector, approximately in the
 645 longitude stretch between India and western Australia. In terms of net heat flux pertur-
 646 bations, in the Pacific sector we suggest applying perturbations south of the RVP sur-
 647 face projection and north of the SAF (or a suitable SSH proxy), while still in the region
 648 of deep mixed layers. In the Indian sector, we suggest perturbations (1) south of New
 649 Zealand and north of the SAF or (2) just south of the SAF proxy. The comprehensive
 650 sensitivity study carried out here suggests that RVPPh is only weakly sensitive to net heat
 651 flux or wind stress anomalies south of the SAF on the 10-15 year timescales considered
 652 here.

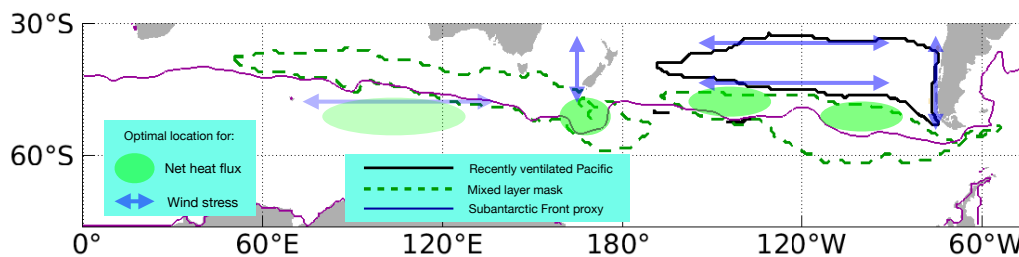


Figure 14. Summary schematic of optimal locations for perturbation experiments. The regions in the Indian sector are more opaque because they are expected to produce weaker responses, at least on the 10-year timescale, compared with perturbations in the Pacific sector.

Appendix A Separating linear and non-linear responses

We separate the linear and non-linear responses of a given quantity by imposing positive and negative perturbations of the same magnitude in two different model runs following Verdy et al. (2014) and Jones et al. (2018). Given a perturbation $\Delta Q = Q - Q_0$, in a quantity Q , then the response of a variable $H(Q)$ can be approximated by Taylor series expansions as:

$$\Delta H = H - H_0 = \frac{\partial H}{\partial Q}(Q - Q_0) + \frac{1}{2} \frac{\partial^2 H}{\partial Q^2}(Q - Q_0)^2 + \dots, \quad (\text{A1})$$

where H_0 and Q_0 are reference values about which the partial derivatives are evaluated. We denote the response to a positive perturbation $Q > Q_0$ as ΔH_+ and the response to a negative perturbation $Q < Q_0$ as ΔH_- . We then estimate the linear response by the difference $(\Delta H_+ - \Delta H_-)/2 \approx (\partial_Q H)(Q - Q_0)$ and the non-linear response by the sum $(\Delta H_+ + \Delta H_-)/2 \approx 0.5(\partial_{QQ} H)(Q - Q_0)^2$. This approach is expected to work well if the response function in question can be well represented by a Taylor series expansion and if the first two non-constant terms capture the majority of the variability of that response function.

Acronyms

ACC Antarctic Circumpolar Current

AAIW Antarctic Intermediate Water

MLD Mixed layer depth

SPG South Pacific Gyre

RVP Recently ventilated Pacific sector of the Southern Ocean (fixed volume)

RVP_h Heat content of the fixed-volume RVP

SAF Subantarctic Front

SAMW Subantarctic Mode Water

SO Southern Ocean

SSH Sea surface height

Acknowledgments

This study is supported by grants from the Natural Environment Research Council (NERC), including [1] The North Atlantic Climate System Integrated Study (ACSIS) (grant NE/N018028/1,

681 authors DJ, ES), [2] Securing Multidisciplinary UndeRstanding and Prediction of Hia-
 682 tus and Surge events (SMURPHS) (grant NE/N006038/1, author EB), and [3] Ocean
 683 Regulation of Climate by Heat and Carbon Sequestration and Transports (ORCHES-
 684 TRA) (grant NE/N018095/1, authors EB, AM). GF is supported by NASA award #6937342
 685 and Simons Foundation award #549931. The ECCOv4-r2 model setup used in this work
 686 is available for download on Github (<https://github.com/gaelforget/ECCOv4>) as an
 687 instance of the MIT general circulation model (MITgcm, <http://mitgcm.org/>). Nu-
 688 merical model runs were carried out on ARCHER, the UK national HPC facility [[http://](http://archer.ac.uk/)
 689 archer.ac.uk/]. Adjoint code was generated using the TAF software tool, created and
 690 maintained by FastOpt GmbH [<http://www.fastopt.com/>].

691 References

- 692 Cerovečki, I., & Mazloff, M. (2015). The spatiotemporal structure of dia-
 693 batic processes governing the evolution of Subantarctic Mode Water in the
 694 Southern Ocean. *Journal of Physical Oceanography*, *46*, 683–710. doi:
 695 10.1175/JPO-D-14-0243.1
- 696 Cerovecki, I., Meijers, A. J. S., Mazloff, M. R., Gille, S. T., Tamsitt, V. M., Holland,
 697 P. R., & Tamsitt, V. M. (2019). The effects of enhanced sea ice export from
 698 the Ross Sea on recent cooling and freshening of the Southeast Pacific. *Journal*
 699 *of Climate*, JCLI-D-18-0205.1. doi: 10.1175/JCLI-D-18-0205.1
- 700 Cerovecki, I., Talley, L. D., Mazloff, M. R., & Maze, G. (2013). Subantarctic Mode
 701 Water Formation, Destruction, and Export in the Eddy-Permitting Southern
 702 Ocean State Estimate. *Journal of Physical Oceanography*, *43*(7), 1485–1511.
 703 doi: 10.1175/jpo-d-12-0121.1
- 704 Cessi, P., & Otheguy, P. (2003). Oceanic teleconnections: Remote response to
 705 decadal wind forcing. *Journal of Physical Oceanography*, *33*(8), 1604–1617.
- 706 Dee, D. P., Uppala, S. M., Simmons, A. J., Berrisford, P., Poli, P., Kobayashi, S., ...
 707 Vitart, F. (2011). The ERA-Interim reanalysis: configuration and performance
 708 of the data assimilation system. *Quarterly Journal of the Royal Meteorological*
 709 *Society*, *137*(656), 553–597. doi: 10.1002/qj.828
- 710 Downes, S. M., Bindoff, N. L., Downes, S. M., Bindoff, N. L., & Rintoul, S. R.
 711 (2009). Impacts of Climate Change on the Subduction of Mode and Intermedi-
 712 ate Water Masses in the Southern Ocean. *dx.doi.org*, *22*(12), 3289–3302 PB –.

- 713 doi: 10.1175/2008JCLI2653.1
- 714 Fekete, B. M., Vörösmarty, C. J., & Grabs, W. (2002). High-resolution fields
715 of global runoff combining observed river discharge and simulated wa-
716 ter balances. *Global Biogeochemical Cycles*, *16*(3), 15–1–15–10. doi:
717 10.1029/1999GB001254
- 718 Forget, G., Campin, J. M., Heimbach, P., Hill, C. N., Ponte, R. M., & Wunsch, C.
719 (2015). ECCO version 4: an integrated framework for non-linear inverse mod-
720 eling and global ocean state estimation. *Geoscientific Model Development*,
721 *8*(10), 3071–3104. doi: 10.5194/gmd-8-3071-2015
- 722 Forget, G., Ferreira, D., & Liang, X. (2015). On the observability of turbulent trans-
723 port rates by Argo: supporting evidence from an inversion experiment. *Ocean*
724 *Science Discussions*, *12*(3), 1107–1143. doi: 10.5194/osd-12-1107-2015
- 725 Frölicher, T. L., Sarmiento, J. L., Paynter, D. J., Dunne, J. P., Krasting, J. P., &
726 Winton, M. (2015). Dominance of the Southern Ocean in Anthropogenic Car-
727 bon and Heat Uptake in CMIP5 Models. *Journal of Climate*, *28*(2), 862–886.
728 doi: 10.1175/jcli-d-14-00117.1
- 729 Gao, L., Rintoul, S. R., & Yu, W. (2018). Recent wind-driven change in Subantarctic
730 Mode Water and its impact on ocean heat storage. *Nature Publishing*
731 *Group*, 1–7. doi: 10.1038/s41558-017-0022-8
- 732 Garabato, A. C. N., Jullion, L., Stevens, D. P., Heywood, K. J., & King, B. A.
733 (2009).
734 *Journal of Climate*, *22*(13), 3661–3688. doi: 10.1175/2009jcli2621.1
- 735 Gaspar, P., Grégoris, Y., & Lefevre, J. M. (1990). A simple eddy kinetic energy
736 model for simulations of the oceanic vertical mixing: Tests at station Papa and
737 long-term upper ocean study site. *Journal of Geophysical Research: Atmo-*
738 *spheres*, *95*(C9), 16179–16193. doi: 10.1029/JC095iC09p16179
- 739 Gent, P. R., & McWilliams, J. C. (1990). Isopycnal Mixing in Ocean Circulation
740 Models. *Journal of Physical Oceanography*, *20*(1), 150–155. doi: 10.1175/1520-
741 -0485(1990)020<0150:imiocm>2.0.co;2
- 742 Hanawa, K., & Talley, L. (2001). Mode Waters. In G. Siedler & J. Church (Eds.),
743 *Ocean circulation and climate* (pp. 373–386). International Geophysics Series.
- 744 Herraiz-Borreguero, L., & Rintoul, S. R. (2011). Subantarctic mode water: distri-
745 bution and circulation. *Ocean Dynamics*, *61*(1), 103–126. doi: 10.1007/s10236

746 -010-0352-9

- 747 Hyder, P., Edwards, J. M., Allan, R. P., Hewitt, H. T., Bracegirdle, T. J., Gregory,
 748 J. M., ... Belcher, S. E. (2018). Critical Southern Ocean climate model biases
 749 traced to atmospheric model cloud errors. *Nature Communications*, 1–17. doi:
 750 10.1038/s41467-018-05634-2
- 751 Ito, T., Woloszyn, M., & Mazloff, M. (2010). Anthropogenic carbon dioxide trans-
 752 port in the Southern Ocean driven by Ekman flow. *Nature*, 463, 80. doi: 10
 753 .1038/nature08687
- 754 Iudicone, D., Rodgers, K., Schopp, R., & Madec, G. (2007). An exchange win-
 755 dow for the injection of Antarctic Intermediate Water into the South Pacific.
 756 *Journal of Physical Oceanography*, 37, 31–49. doi: [http://dx.doi.org/10.1175/
 757 JPO2985.1](http://dx.doi.org/10.1175/JPO2985.1)
- 758 Jones, D. C., Forget, G., Sinha, B., Josey, S. A., Boland, E. J. D., Meijers, A. J. S.,
 759 & Shuckburgh, E. (2018). Local and Remote Influences on the Heat Content of
 760 the Labrador Sea: An Adjoint Sensitivity Study. *JOURNAL OF GEOPHYSI-
 761 CAL RESEARCH-OCEANS*, 105(2-3), 182. doi: 10.1002/2018JC013774
- 762 Jones, D. C., Meijers, A. J. S., Shuckburgh, E., Sallée, J.-B., Haynes, P., McAufield,
 763 E. K., & Mazloff, M. R. (2016). How does Subantarctic Mode Water venti-
 764 late the Southern Hemisphere subtropics? *JOURNAL OF GEOPHYSICAL
 765 RESEARCH-OCEANS*, 121(9), 6558–6582. doi: 10.1002/2016jc011680
- 766 Kalnay, E., Kanamitsu, M., Kistler, R., Collins, W., Deaven, D., Gandin, L., ...
 767 Woollen, J. (1996). The NCEP/NCAR 40-year reanalysis project. *Bulletin of
 768 the American Meteorological Society*, 77(3), 437–471.
- 769 Kara, A., & Rochford, P. (2003). Mixed layer depth variability over the global
 770 ocean. *Journal of Geophysical Research - Oceans*.
- 771 Karsten, R., & Marshall, J. (2002). Testing theories of the vertical stratification
 772 of the ACC against observations. *Dynamics of Atmospheres and Oceans*, 36,
 773 233–246.
- 774 Khatiwala, S., Primeau, F., & Hall, T. (2009). Reconstruction of the history of
 775 anthropogenic CO₂ concentrations in the ocean. *Nature*, 462(7271), 346–349.
 776 doi: 10.1038/nature08526
- 777 Large, W., & Yeager, S. (2009). The global climatology of an interannually varying
 778 air–sea flux data set. *Climate Dynamics*, 33, 341–364. doi: 10.1007/s00382-008

779 -0441-3

- 780 Liu, L., & Huang, R. (2012). The global subduction/obduction rates: Their interan-
 781 nual and decadal variability. *Journal of Climate*, *25*, 1096–1115. doi: 10.1175/
 782 2011JCLI4228.1
- 783 Losch, M., Menemenlis, D., Campin, J.-M., Heimbach, P., & Hill, C. (2010). On
 784 the formulation of sea-ice models. Part 1: Effects of different solver imple-
 785 mentations and parameterizations. *Ocean Modelling*, *33*(1-2), 129–144. doi:
 786 10.1016/j.ocemod.2009.12.008
- 787 Lovenduski, N., & Ito, T. (2009). The future evolution of the Southern Ocean CO₂
 788 sink. *Journal of Marine Research*, *67*, 597–617.
- 789 Lumpkin, R., & Speer, K. (2007). Global ocean meridional overturning. *Journal of*
 790 *Physical Oceanography*, *37*, 2550–2562. doi: 10.1175/JPO3130.1
- 791 Marshall, J., & Speer, K. (2012a). Closure of the meridional overturning circulation
 792 through Southern Ocean upwelling. *Nature Geoscience*, *5*(3), 171–180. doi: 10
 793 .1038/ngeo1391
- 794 Marshall, J., & Speer, K. (2012b). Closure of the meridional overturning circulation
 795 through Southern Ocean upwelling. *Nature Geoscience*, *5*, 171–180. doi: 10
 796 .1038/ngeo1391
- 797 Morrison, A., Hogg, A., & Ward, M. L. (2011). Sensitivity of the Southern Ocean
 798 overturning circulation to surface buoyancy forcing. *Geophysical Research Let-*
 799 *ters*, *38*(L14602). doi: 10.1029/2011GL048031
- 800 Rintoul, S. R., & England, M. H. (2002). Ekman Transport Dominates Local
 801 Air–Sea Fluxes in Driving Variability of Subantarctic Mode Water. *Journal*
 802 *of Physical Oceanography*, *32*(5), 1308–1321. doi: 10.1175/1520-0485(2002)
 803 032<1308:etdlas>2.0.co;2
- 804 Russell, J., Dixon, K., Gnanadesikan, A., Stouffer, R., & Toggweiler, J. (2006). The
 805 Southern Hemisphere westerlies in a warming world: Propping open the door
 806 to the deep ocean. *Journal of Climate*, *19*, 6382–6390.
- 807 Sabine, C., Feely, R., Gruber, N., Key, R., Lee, K., Bullister, J. L., . . . Rios, A. F.
 808 (2004). The oceanic sink for anthropogenic CO₂. *Science*, *305*(367). doi:
 809 10.1126/science.1097403
- 810 Sallée, J., & Rintoul, S. (2011). Parameterization of eddy-induced subduction in the
 811 Southern Ocean surface-layer. *Ocean Modelling*, *39*, 146–153.

- 812 Sallée, J., Speer, K., Rintoul, S., & Wijffels, S. (2010). Southern Ocean thermocline
813 ventilation. *Journal of Physical Oceanography*, *40*, 509–529.
- 814 Sallée, J.-B., Matear, R. J., Rintoul, S. R., & Lenton, A. (2012). Localized subduc-
815 tion of anthropogenic carbon dioxide in the Southern Hemisphere oceans. *Nature*
816 *Geoscience*, *5*(8), 579–584. doi: 10.1038/ngeo1523
- 817 Sallée, J.-B., Speer, K., Rintoul, S., & Wijffels, S. (2010). Southern Ocean Thermo-
818 cline Ventilation. *Journal of Physical Oceanography*, *40*(3), 509–529. doi: 10
819 .1175/2009jpo4291.1
- 820 Sarmiento, J. L., Gruber, N., Brzezinski, M. A., & Dunne, J. P. (2004). High-
821 latitude controls of thermocline nutrients and low latitude biological productiv-
822 ity. *Nature*, *427*(6969), 56–60. doi: 10.1038/nature02127
- 823 Speer, K., & Forget, G. (2013). Global Distribution and Formation of Mode Wa-
824 ters. In *Ocean circulation and climate - a 21st century perspective* (pp. 211–
825 226). Elsevier. doi: 10.1016/B978-0-12-391851-2.00009-X
- 826 Speer, K., Rintoul, S., & Sloyan, B. (2000). The Diabatic Deacon Cell. *Journal of*
827 *Physical Oceanography*, *30*(12), 3212–3222.
- 828 Talley, L. (2008). Freshwater transport estimates and the global overturning circu-
829 lation: Shallow, deep and throughflow components. *Progress in Oceanography*,
830 *78*(3), 257–303. doi: 10.1016/j.pocean.2008.05.001
- 831 Verdy, A., Mazloff, M. R., Cornuelle, B. D., & Kim, S. Y. (2014). Wind-
832 Driven Sea Level Variability on the California Coast: An Adjoint Sensi-
833 tivity Analysis. *Journal of Physical Oceanography*, *44*(1), 297–318. doi:
834 10.1175/JPO-D-13-018.1